Grating integrated single mode microring laser

Amir Arbabi,[1,2] Seyedeh Mahsa Kamali,[1,2] Ehsan Arbabi,[1,2] Benjamin G. Griffin,[1,3,4] and Lynford L. Goddard[1,*]

[1]*Department of Electrical and Computer Engineering, Micro and Nanotechnology Laboratory, University of Illinois at Urbana-Champaign, 208 North Wright Street Urbana, IL 61801, USA*

[2]*T. J. Watson Laboratory of Applied Physics, California Institute of Technology, 1200 E California Blvd., Pasadena, CA 91125, USA*

[3]*UES, Inc., Dayton, OH 45432, USA*

[4]*Air Force Research Laboratory, Wright-Patterson Air Force Base, OH 45433, USA*

[*]*lgoddard@illinois.edu*

Abstract: Microring and microdisk lasers are potential candidates for small footprint, low threshold in-plane integrated lasers; however, they exhibit multimode lasing spectra and bistability. Here, we theoretically propose and experimentally demonstrate a novel approach for achieving single mode lasing in microring lasers. Our approach is based on increasing the radiation loss of all but one of the resonant modes of microring resonators by integrating second order gratings on the microrings' waveguide. We present single mode operation of electrically pumped semiconductor microring lasers whose lasing modes are lithographically selected via the second order grating. We also show that adding the grating does not increase the lasing threshold current significantly.

OCIS codes: (140.5960) Semiconductor lasers; (050.2770) Gratings; (140.4780) Optical resonators; (140.3948) Microcavity devices.

References and links

1. S. L. McCall, A. F. J. Levi, R. E. Slusher, S. J. Pearton, and R. A. Logan, "Whispering-gallery mode microdisk lasers," Appl. Phys. Lett. **60**, 289 (1992).
2. K. Amarnath, R. Grover, and S. Kanakaraju, "Electrically pumped InGaAsP-InP microring optical amplifiers and lasers with surface passivation," IEEE Photon. Technol. Lett. **17**, 2280–2282 (2005).
3. A. Bennecer, K. A. Williams, R. V. Penty, I. H. White, M. Hamacher, and H. Heidrich, "Directly modulated wavelength-multiplexed integrated microring laser array," IEEE Photon. Technol. Lett. **20**, 1411–1413 (2008).
4. J. D. B. Bradley, E. S. Hosseini, Z. Su, T. N. Adam, G. Leake, D. Coolbaugh, and M. R. Watts, "Monolithic erbium- and ytterbium-doped microring lasers on silicon chips," Opt. Express **22**, 12226 (2014).
5. M. Fujita and T. Baba, "Microgear laser," Appl. Phys. Lett. **80**, 2051 (2002).
6. M. T. Hill, S. Anantathanasarn, Y. Zhu, Y. S. Oei, P. J. Van Veldhoven, M. K. Smit, and R. Nötzel, "InAs-InP (1.55-μm region) quantum-dot microring lasers," IEEE Photon. Technol. Lett. **20**, 446–448 (2008).
7. A. Kapsalis, I. Stamataki, C. Mesaritakis, D. Syvridis, M. Hamacher, and H. Heidrich, "Design and experimental evaluation of active-passive integrated microring lasers: noise properties," IEEE J. Quantum Electron. **48**, 99–106 (2012).
8. A. Kapsalis, I. Stamataki, C. Mesaritakis, D. Syvridis, M. Hamacher, and H. Heidrich, "Design and experimental evaluation of active-passive integrated microring lasers: threshold current and spectral properties," IEEE J. Quantum Electron. **47**, 1557–1564 (2011).
9. A. Kapsalis, I. Stamataki, S. Mikroulis, D. Syvridis, and M. Hamacher, "Widely tunable all-active microring lasers," IEEE Photon. Technol. Lett. **18**, 2641–2643 (2006).

#231409 - $15.00 USD Received 26 Dec 2014; revised 6 Feb 2015; accepted 6 Feb 2015; published 20 Feb 2015

10. N. Kryzhanovskaya, I. Mukhin, E. Moiseev, I. Shostak, A. Bogdanov, A. Nadtochiy, M. Maximov, A. Zhukov, M. Kulagina, K. Vashanova, Y. Zadiranov, S. Troshkov, A. Lipovskii, and A. Mintairov, "Control of emission spectra in quantum dot microdisk/microring lasers," Opt. Express **22**, 25782 (2014).
11. D. Liang, M. Fiorentino, T. Okumura, H.-H. Chang, D. T. Spencer, Y.-H. Kuo, A. W. Fang, D. Dai, R. G. Beausoleil, and J. E. Bowers, "Electrically-pumped compact hybrid silicon microring lasers for optical interconnects," Opt. Express **17**, 20355–20364 (2009).
12. K. Nozaki, A. Nakagawa, D. Sano, and T. Baba, "Ultralow threshold and single-mode lasing in microgear lasers and its fusion with quasi-periodic photonic crystals," IEEE J. Sel. Top. Quantum Electron. **9**, 1355–1360 (2003).
13. J. S. Parker, E. J. Norberg, Y.-J. Hung, B. Kim, R. S. Guzzon, and L. A. Coldren, "InP/InGaAsP flattened ring lasers with low-loss etched beam splitters," IEEE Photon. Technol. Lett. **23**, 573–575 (2011).
14. L. Shang, L. Liu, and L. Xu, "Single-frequency coupled asymmetric microcavity laser," Opt. Express **33**, 1150 (2008).
15. G. Mezosi, M. J. Strain, S. Furst, and M. Sorel, "Bistable micro-ring lasers with compact footprint and high output efficiency," IEEE J. Quantum Electron. **48**, 1023–1030 (2012).
16. I. Stamataki, S. Mikroulis, A. Kapsalis, and D. Syvridis, "Investigation on the multimode dynamics of InGaAsPInP microring lasers," IEEE J. Quantum Electron. **42**, 1266–1273 (2006).
17. K. E. Chlouverakis, S. Mikroulis, I. Stamataki, and D. Syvridis, "Chaotic dynamics of semiconductor microring lasers," Opt. Lett. **32**, 2912 (2007).
18. M. T. Hill, H. J. S. Dorren, T. De Vries, X. J. M. Leijtens, J. H. Den Besten, B. Smalbrugge, Y.-S. Oei, H. Binsma, G.-D. Khoe, and M. K. Smit, "A fast low-power optical memory based on coupled micro-ring lasers," Nature (London) **432**, 206–209 (2004).
19. L. Liu, R. Kumar, K. Huybrechts, T. Spuesens, G. Roelkens, E.-J. Geluk, T. de Vries, P. Regreny, D. Van Thourhout, R. Baets, and G. Morthier, "An ultra-small, low-power, all-optical flip-flop memory on a silicon chip," Nature Photon. **4**, 182–187 (2010).
20. S. Srinivasan, D. A. Fattal, M. Fiorentino, D. T. Spencer, J. E. Bowers, and R. G. Beausoleil, "Teardrop reflector-assisted unidirectional hybrid silicon microring lasers," IEEE Photon. Technol. Lett. **24**, 1988–1990 (2012).
21. L. Feng, Z. J. Wong, R.-M. Ma, Y. Wang, and X. Zhang, "Single-mode laser by parity-time symmetry breaking," Science **346**, 972–975 (2014).
22. Y. M. Kang, A. Arbabi, and L. L. Goddard, "Engineering the spectral reflectance of microring resonators with integrated reflective elements," Opt. Express **18**, 16813–16825 (2010).
23. A. Arbabi, Y. M. Kang, and L. L. Goddard, "Cylindrical coordinates coupled mode theory," IEEE J. Quantum Electron. **46**, 1769–1774 (2010).
24. A. Arbabi, Y. M. Kang, C.-Y. Lu, E. Chow, and L. L. Goddard, "Realization of a narrowband single wavelength microring mirror," Appl. Phys. Lett. **99**, 091105 (2011).
25. M.-F. Xue, Y. M. Kang, A. Arbabi, S. J. McKeown, L. L. Goddard, and J.-M. Jin, "Fast and accurate finite element analysis of large-scale three-dimensional photonic devices with a robust domain decomposition method," Opt. Express **22**, 4437–4452 (2014).
26. A. Arbabi and L. L. Goddard, "Single Wavelength Microring Laser," in "CLEO: 2013," (OSA, Washington, D.C., 2013), p. CM3F.2.
27. A. Arbabi and L. L. Goddard, "Grating assisted mode coupling in microring resonators," in "2013 IEEE Photonics Conference," (IEEE, 2013), pp. 434–435.
28. J. D. Jackson, *Classical Electrodynamics,* 3rd ed. (Wiley, 1999).
29. A. Arbabi and S. Safavi-Naeini, "Maximum gain of a lossy antenna," IEEE Trans. Antennas Propag. **60**, 2–7 (2012).
30. A. Devaney and E. Wolf, "Radiating and nonradiating classical current distributions and the fields they generate," Phys. Rev. D **8**, 1044–1047 (1973).

1. Introduction

Semiconductor lasers with small footprint, low threshold current, in-plane emission, and moderate output power are highly desirable in photonic integrated circuits, on-chip optical interconnects, and short distance optical communication. Microdisk and microring lasers coupled to bus waveguides possess these characteristics and are promising candidates for such applications. Several demonstrations of microring and microdisk lasers have been reported [1–15], but they are generally multimode and suffer from bistable lasing of two degenerate counter-propagating modes [15–17]. For achieving practical output powers, the radius of a microdisk or microring laser should be in the tens of microns range. Such a laser cavity has closely spaced high quality factor modes of different azimuthal orders; therefore, the laser operates in the multimode lasing regime. Furthermore, the existence of two degenerate modes at each resonant

#231409 - $15.00 USD Received 26 Dec 2014; revised 6 Feb 2015; accepted 6 Feb 2015; published 20 Feb 2015

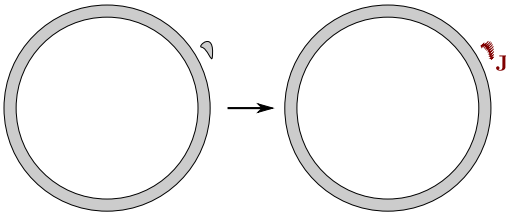

Fig. 1. Schematic illustration of a microring resonator with a small refractive index perturbation. The perturbation can be replaced with an equivalent volume current.

wavelength leads to bistable lasing in these micro-lasers. Although the bistable behavior can be useful in designing optical memory devices [18, 19], it is generally not a desirable characteristic for a laser source.

Several techniques have been investigated for breaking the degeneracy and achieving stable lasing characteristics [20, 21]. Patterning first order gratings on microdisks with small diameters has been shown to increase their radiation quality factors [5]. Such gratings couple the two counterpropagating modes to each other significantly [22–24] and may scatter some of the light to radiation modes of larger azimuthal orders which have higher quality factors; however, they do not affect the quality factors of resonant modes of microrings and microdisks with large diameters significantly [25]. It has been recently demonstrated that a metallic grating can be used to decrease the quality factors of different modes of a microring resonator by different amounts, and an optically pumped single mode microring laser has been reported using a metallic grating [21]. Nevertheless, the metallic grating introduces substantial absorption loss to the lasing mode and increases its threshold power. Recently, we reported single mode lasing in a microring resonator with a second order grating [26, 27]. Here, we present a detailed theoretical analysis and experimental validation which show how a second order azimuthal grating patterned on the microring reduces the quality factors of all but one of the microring resonant modes. As we show, the grating will inflict significant radiation loss to all modes with different azimuthal orders from the azimuthal order of the grating. Furthermore, out of the two degenerate modes with the same azimuthal order as the grating, one will radiate significantly while the low radiation loss of the other one is preserved. As a result, the second order grating patterned microring or microdisk cavities have only one high quality factor mode. This mode will be the one that lases when the cavity is pumped.

In section 2, we present a method for analyzing the radiation caused by a small refractive index perturbation to a microring resonator. Using this method, we estimate the radiation loss of microring resonant modes in the presence of the index perturbation of an azimuthal grating. We also present numerical simulation results of a microring resonator with a second order grating. We present design and fabrication details in section 3, and discuss the measurement results in section 4.

2. Analysis of radiation from microring resonators with gratings

To estimate the radiation loss modification caused by adding a grating to a microring resonator, we consider the grating as a permittivity perturbation to the plain microring resonator. As shown schematically in Fig. 1, a permittivity perturbation to a microring resonator can be modeled as an equivalent volume current density which is proportional to the product of the electric field of the microring and the permittivity perturbation (see Appendix A). If we assume that the perturbation is small and the fields for the perturbed structure can be approximated by those of the unperturbed structure, then the radiation from the perturbed resonator will be dominated by

#231409 - $15.00 USD Received 26 Dec 2014; revised 6 Feb 2015; accepted 6 Feb 2015; published 20 Feb 2015

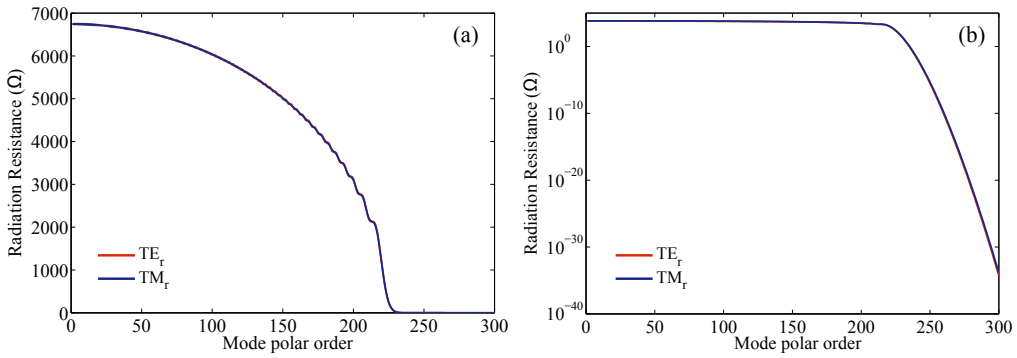

Fig. 2. (a) Radiation resistance of multipole modes. Radiation resistance for the TE and TM modes of the same polar order are almost equal to each other. (b) Radiation resistance on a log scale. The radiation resistance values drop fast for $l > kR$.

the radiation of the equivalent volume current.

To provide an intuitive understanding of how a second order grating causes radiation loss to different modes of a microring, we use the multipole expansion method. In this method, the optical waves outside the microring are expanded in spherical coordinates in terms of the fields of the electric and magnetic multipoles of different orders, which radiate transverse magnetic (TM) and transverse electric (TE) waves, respectively [28]. The total power radiated by the equivalent volume current is the summation of the power radiated by each individual multipole order [28], that is

$$P = \sum_{l=1}^{\infty} \sum_{m=-l}^{l} P_{lm}^{\mathrm{TM}} + P_{lm}^{\mathrm{TE}}, \tag{1}$$

where P_{lm}^{TM} and P_{lm}^{TE} are the radiated power into the TM and TE multipoles for the polar and azimuthal order (l,m), respectively. Note that the summation starts from $l = 1$ since the monopole term only exists for electrostatic fields. As we have shown in Appendix A, for both TE and TM multipoles, the power radiated can be expressed as

$$P_{lm}^{\mathrm{TM/TE}} = \frac{1}{2} R_l^{\mathrm{TM/TE}} I_{lm}^{\mathrm{TM/TE}^2}, \tag{2}$$

where $I_{lm}^{\mathrm{TM/TE}}$ is the norm of the component of the equivalent volume current that excites the multipole of order (l,m). $I_{lm}^{\mathrm{TM/TE}}$ and $R_l^{\mathrm{TM/TE}}$ have the same units as electric current and resistance, respectively. We refer to $R_l^{\mathrm{TM/TE}}$ as radiation resistance of the multipoles. Equation (2) resembles the power dissipation relation of a resistor, and it provides an intuitive picture for the power radiated by a volume current. According to this picture, any volume current can be expanded as a superposition of orthogonal components that excite different multipoles plus a component that does not radiate (see Appendix A for details). The total radiated power is the summation of the powers radiated by each multipole. The power radiated by each of these modes is related to the strength of excitation of that multipole (i.e. norm of the corresponding current component in the expansion), and a radiation resistance. For equal excitations, multipoles with large radiation resistance radiate more than the ones with small radiation resistance.

Note that radiation resistance depends only on the polar order of the multipole (l) and is independent of its azimuthal order (m) (see Appendix A). The radiation resistance of multipole modes as a function of l is shown in Fig. 2(a). In this figure, $kR = 225$ where k is the wavenumber in vacuum, and R is the radius of the smallest sphere that encloses the microring resonator.

#231409 - $15.00 USD Received 26 Dec 2014; revised 6 Feb 2015; accepted 6 Feb 2015; published 20 Feb 2015

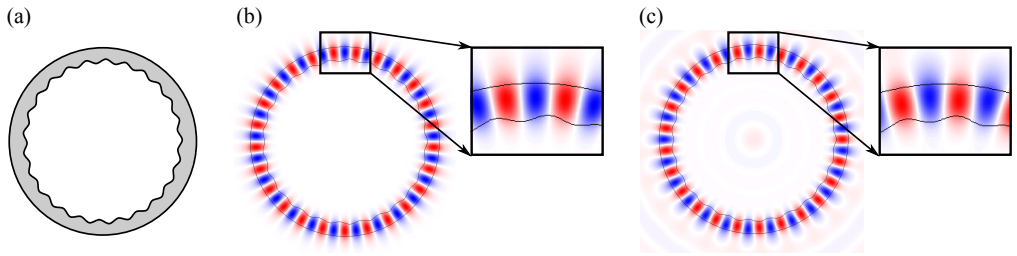

Fig. 3. (a) Schematic illustration of a microring resonator with an azimuthal grating. (b) Electric field distribution of the non-radiating and (c) radiating resonant modes with the same azimuthal order as the grating. The insets in (b) and (c) show the zoomed in views of the simulations and the locations of the electrical field nodes and antinodes with respect to grating indentations.

The same plot is presented using a semi-log scale in Fig. 2(b). As can be seen from Figs. 2(a) and 2(b), the radiation resistance has a cut-off value around $l = kR$, and modes with $l > kR$ radiate inefficiently. Finally, we note that in the modal expansion the azimuthal order is limited to $|m| \leq l$. Therefore, a current density with large azimuthal order (i.e. $|m|$ large compared to kR) does not radiate efficiently because $l \geq |m| > kR$, while a current density with small m might radiate significantly. This is the main conclusion of this analysis. It gives us an intuitive understanding of the radiation characteristics of a microring with an azimuthal grating.

Now we consider a microring resonator integrated with a grating with azimuthal order M as shown schematically in Fig. 3(a), and study the grating induced radiation loss of its resonant modes with azimuthal order m. As we mentioned earlier, the equivalent current density is proportional to the product of the electric field of the plain microring (i.e. the microring without the grating) and the permittivity perturbation; therefore, the current density has azimuthal harmonics with orders $m-M$ and $m+M$. For modes close to the $m = M$ mode, $m-M$ is a small number and the $m-M$ azimuthal order component of the volume current radiates significantly; as a result, the quality factors of these microring modes are reduced. The only exception happens for one of the standing resonant modes of azimuthal order $m = M$ whose electric field is shifted by $\lambda/4$ compared to the first harmonic of the periodic permittivity perturbation that defines the grating (see Fig. 3(b)). Assuming the first harmonic of the grating permittivity perturbation has the ϕ dependence in the form of $\cos(M\phi)$, the peak of the electric field of the non-radiating mode is shifted by $\lambda/4$ and has ϕ dependence in the form of $\sin(M\phi)$. Thus, the equivalent volume current density for this mode is proportional to $\sin(M\phi) \times \cos(M\phi) = 1/2\sin(2M\phi)$ which has zero amplitude for the harmonic at $m-M = 0$; therefore, its radiation quality factor is not affected by the grating.

To confirm that adding a second order grating reduces the quality factors of all modes of a microring resonator except for one, we performed numerical simulations using Finite Element Method (FEM), and found the resonant modes of a 2D microring resonator integrated with a second order grating. Figure 3(a) shows a schematic illustration of the simulated device. The outer microring radius is 2.345 μm, the waveguide width is sinusoidally modulated and varies between 340+d nm and 340-d nm where d is the indentation depth in nanometers. The refractive index of the microring waveguide's core and cladding are assumed to be equal to 2 and 1, respectively. The azimuthal order of the grating was chosen to be M=25 such that the microring resonance with azimuthal order $m = M$ has a wavelength of approximately 985 nm. The electric field distributions for the non-radiating and radiating modes of the microring are shown in Figs. 3(b) and 3(c), respectively. The log-scale amplitudes of the electric fields for a few modes close to the $m = M$ mode are shown in Fig. 4(a). In Fig. 4(a), for each value of

#231409 - $15.00 USD Received 26 Dec 2014; revised 6 Feb 2015; accepted 6 Feb 2015; published 20 Feb 2015

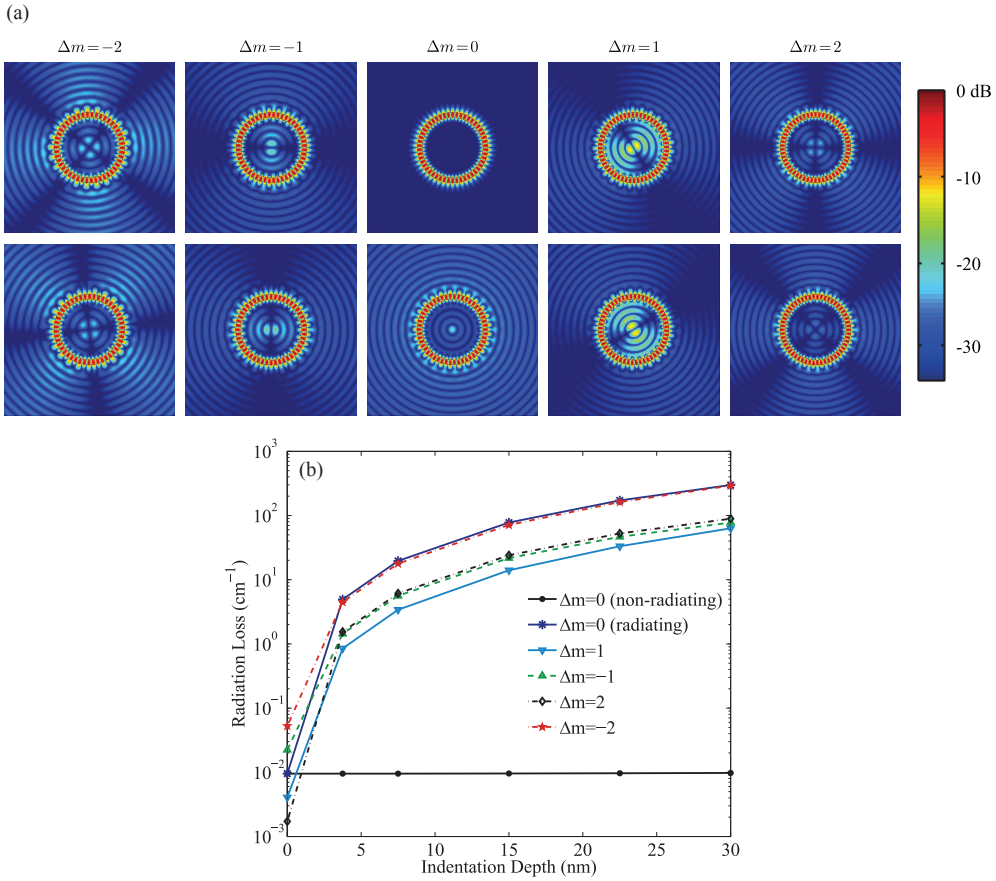

Fig. 4. (a) Simulated logarithmic scale electric field amplitudes of resonant modes of a microring with second order grating at their corresponding resonant wavelengths. $\Delta m = m - M$ represents the difference between the azimuthal order of the mode and that of the grating. Notice that for each value of Δm there are two modes in each column due to the two originally degenerate modes of the plain microring. (b) Radiation loss of the modes presented in (a) as a function of grating indentation depth.

#231409 - $15.00 USD Received 26 Dec 2014; revised 6 Feb 2015; accepted 6 Feb 2015; published 20 Feb 2015

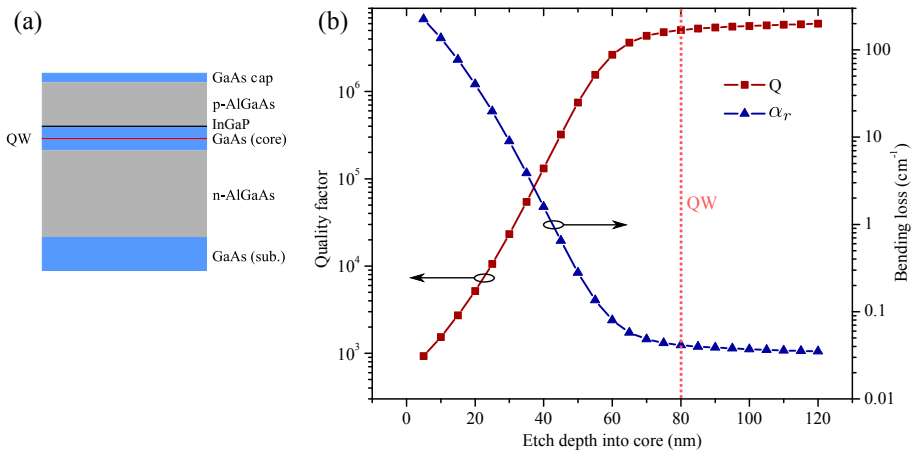

Fig. 5. (a) Epi-layer structure used for fabrication of a single mode microring laser. (b) Dependence of the radiation quality factor and bending loss on the etch depth into the GaAs core. Location of the quantum well (QW) is represented by a vertical dotted line in (b).

$\Delta m = m - M$, two electric field amplitude patterns are shown. These two patterns arise because the plain microring had two degenerate modes for each m, i.e. the clockwise mode and the counterclockwise mode or equivalently, the $\sin(m\phi)$ and the $\cos(m\phi)$ standing wave modes in a different basis. The two patterns for the grating integrated microring with the same value of Δm are shown in the same column. As expected, the radiation patterns show dominant azimuthal dependence of order Δm, and one of the modes with $\Delta m = 0$ radiates significantly less than the others. For each nonzero value of Δm, there are two degenerate modes that differ only by a rotation. The radiation loss versus the grating indentation depth of the modes shown in Fig. 4(a) are computed from the quality factors of these resonant modes, and are presented in Fig. 4(b). For a plain microring (zero grating indentation depth), all the modes have a small radiation loss and the lasing wavelength of a microring laser will be determined by the peak of the gain spectrum. As the indentation depth increases, the radiation losses of all but the main resonant mode increase significantly. For 30 nm indentation depth, the radiation losses of all other modes are larger than 40 cm^{-1}, which is sufficient for single mode operation of the grating-integrated microring laser.

3. Design and fabrication of single mode microring lasers

As a proof of principle, we designed and fabricated plain microring lasers and microring lasers with second order gratings using the epi-layer structure shown in Fig. 5(a). The active layer is a single 8 nm $In_{0.2}Ga_{0.8}As$ quantum well (QW) in the middle of a 160 nm GaAs core region. There is a 5 nm $In_{0.49}Ga_{0.51}P$ layer above the core. That layer was used as a wet etch stop in another project, but is undesirable here. Top and bottom claddings are 500 nm and 1 μm of $Al_{0.8}Ga_{0.2}As$, respectively. The contact layer is 100 nm thick highly doped GaAs and is grown on the top cladding layer. The waveguide width of 1.1 μm, internal microring radius of R_{in}=34.5 μm, and etch depth of 650 nm, i.e. 50 nm into the core, were chosen to minimize bending loss while avoiding etching through the QW which can cause non-radiative surface recombination. The dependence of the bending loss on the etch depth into the core layer is presented in Fig. 5(b). The bending loss is computed from the radiation quality factor of the microring resonant modes, which were found using FEM simulations. A second order

#231409 - $15.00 USD Received 26 Dec 2014; revised 6 Feb 2015; accepted 6 Feb 2015; published 20 Feb 2015

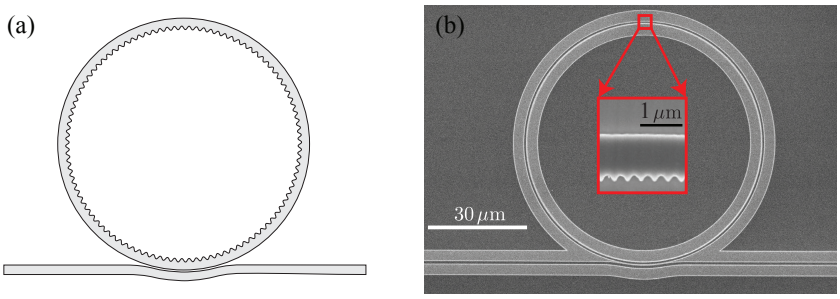

Fig. 6. (a) Schematics of the microring with a second order grating. (b) Scanning electron micrograph of the oxide mask used for etching the device. The inset shows a zoomed in view of the microring waveguide.

sinusoidal grating was created on the microring waveguide by sinusoidally modulating the microring waveguide's width by ±200 nm (as shown in Fig. 6(a)) such that the waveguide width varies between 900 nm and 1300 nm. The 400 nm indentation depth is larger than what we found in 2D simulations presented in section 2 because the waveguide width is larger for the 3D device. Since the device uses a second order grating, an integer multiple of lasing wavelengths (also equal to the grating's azimuthal order M) must fit along the circumference of the microring: $M\lambda/n_{\text{eff}} = 2\pi R_{\text{in}}$, where n_{eff} is the effective index of the microring's waveguide mode found using FEM simulations. For the given radius of 34.5 μm, the choice of M=724 was made to approximately obtain the desired lasing wavelength of λ=985 nm. Note that if n_{eff} varies due to changes in temperature or carrier density, the lasing wavelength will continuously track it, i.e. the laser will tune without mode hopping according to $\lambda = 2\pi R_{\text{in}} n_{\text{eff}}/M$. The coupling gap between the microring and the bus waveguide was set to 50 nm to achieve large out coupling from the microring to the bus waveguide. To further increase the coupling, a section of the bus waveguide was bent around the microring as shown schematically in Fig. 6(a). The microring and the bus waveguides are not phase matched due to the presence of the grating on the microring and the difference in the radius of curvature of the waveguides. By changing the width of the bus waveguide, the two waveguides can be phase matched and the same coupling can be achieved using a larger coupling gap.

To fabricate these devices, we deposited 200 nm of SiO_2 on a sample with the epi-layer structure shown in Fig. 5(a). The device pattern was written using electron beam lithography on a positive resist (ZEP 520A-7). The pattern was transferred from the resist to the SiO_2 layer using dry etch in a 3:1 mixture of CHF_3 and CF_4. Figures 6(a) and 6(b) show the schematics of the device and a scanning electron micrograph of the patterned SiO_2 layer. The patterned SiO_2 was used as a hard mask for etching GaAs/AlGaAs epitaxial layers using inductively coupled plasma reactive ion etching in a mixture of $SiCl_4$, hydrogen, and argon. The etched surface was planarized by spin coating bisbenzocyclobutene (CYCLOTENE 3000 from Dow chemicals), curing it, and performing etch back in a mixture of CF_4 and O_2 plasma. Next, separate contact pads were deposited for injecting currents into the bus waveguides and the microrings. Finally, the backside of the GaAs substrate was lapped and polished and the backside contact metals were deposited.

4. Measurement results and discussion

The devices were pumped by injecting quasi continuous wave (quasi-CW) pulsed current with 2 μs pulse width and 10% duty cycle. The 450 μm long bus waveguide section on the output side of the microring was pumped with 50 mA of current while the 450 μm long segment on the

#231409 - $15.00 USD Received 26 Dec 2014; revised 6 Feb 2015; accepted 6 Feb 2015; published 20 Feb 2015

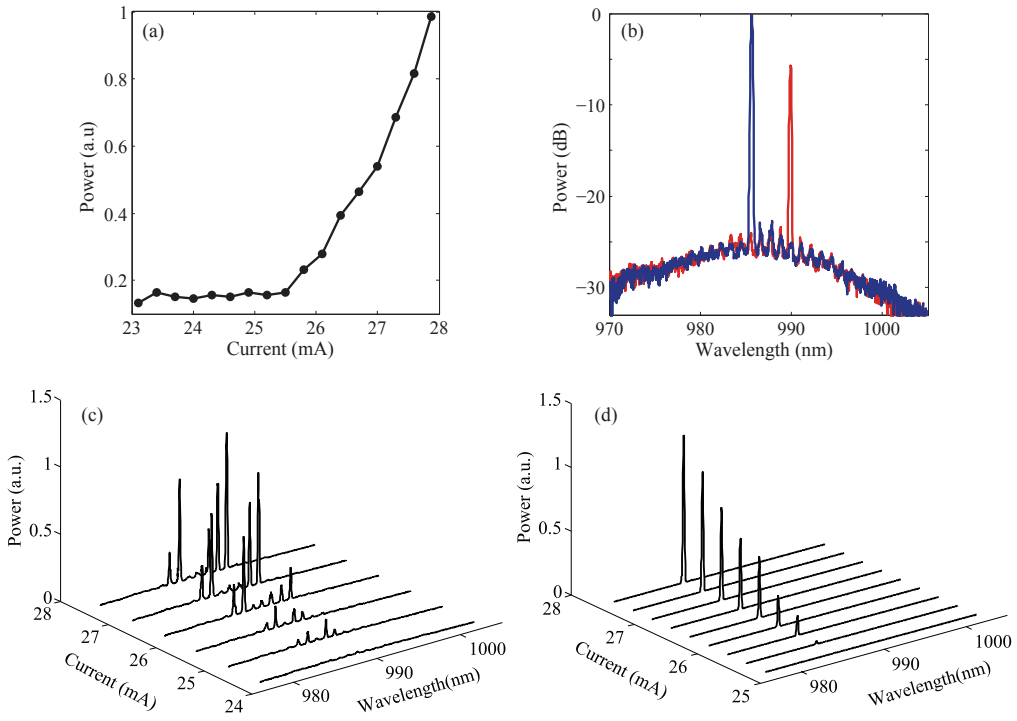

Fig. 7. (a) Output power versus current curve of a grating integrated microring laser with a grating with azimuthal order of M=724. (b) Optical spectra of two grating integrated microring lasers at the same injection currents of 27.5 mA. The azimuthal order of the grating is M=724 for the blue curve, and M=720 for the red curve. (c) Spectra of a microring laser without a grating, and (d) with a grating with azimuthal order of M=724 at different injection currents.

other side was unpumped to prevent lasing in the Fabry-Pérot cavity created by the bus waveguide. The measured L–I curve for a device with a grating order of M=724 is shown in Fig. 7(a). At low microring currents, the measured power is dominated by the spontaneous emission in the bus waveguide and is nonzero at zero bias current of the microring. The spectrum of the device (lasing peak around 985 nm) along with that of another device with M=720 at same injection current of 27.5 mA are shown in Fig. 7(b). As expected, the lasing wavelengths of the two devices are separated by four times the microring's free spectral range, and the lasing wavelengths are selected by the azimuthal orders of the gratings. The lasers with the grating azimuthal orders of M=724 and M=720 have threshold currents of 25.4 mA and 25.9 mA, respectively. By changing the current injected into one side of the bus waveguide, we confirmed that the shape of the spectra is independent from this current and even at zero bus waveguide injection the lasing peak exists; therefore, the emission peak is due to lasing in the microring cavity. The bias voltage for the device with M=724 was approximately 4 V at the bias current of 27.5 mA. The relatively large voltage is mainly due to the presence of the InGaP layer. The measured average laser power coupled to a multimode fiber was 5.4 μW. Considering the 10% duty cycle of the pump current, this corresponds to approximately 0.05% wall plug efficiency. The efficiency can be greatly improved by phase matching the microring and bus waveguides to improve the out coupling of power from the microring.

To demonstrate the effect of the second order grating, the spectrum of a microring laser

#231409 - $15.00 USD Received 26 Dec 2014; revised 6 Feb 2015; accepted 6 Feb 2015; published 20 Feb 2015

without the grating was measured at different microring bias currents and is shown in Fig. 7(c). The measured spectra of the grating integrated device with M=724 is shown in Fig. 7(d) for comparison. Other than the grating, all device parameters are the same between the two devices. As can be seen from Fig. 7(c), the microring laser without the grating starts lasing in the multimode regime while the one with the second order grating exhibits single mode lasing spectra. The threshold current of the microring laser with the grating (I_{th}=25.4 mA) was slightly higher than the laser without it (I_{th}=24.3 mA), which might be due to a small difference in the sidewall roughness. We did not observe power saturation or mode hopping in the lasers with gratings, but the side mode suppression was decreased by approximately 3 dB for the device with lasing wavelength around 985 nm when the pump current was increased from 27.5 mA to 30 mA. Also, the lasers with and without gratings showed comparable output power in this range of current. Due to excessive heating, both devices with and without the grating did not survive pump currents more than approximately 30 mA, even in quasi-CW pulsed mode. We were unable to observe CW lasing due to the additional rise in temperature for CW operation. Removing the InGaP layer will greatly reduce heat generation in the device, while mounting the laser epi-side down on a heat sink will greatly improve heat removal. The main sources of optical loss in the microring cavity are the roughnesses of the sidewall and of the etched planar surface due to the dry etch process since these etched surfaces are close to the waveguide core. Optimizing the waveguide layer design and the dry etch process and coating the etched surface with a layer of silicon nitride are expected to reduce these sources of loss.

In conclusion, we presented a novel approach for making single mode lasers by engineering the radiation quality factors of the laser cavity modes. This approach is fundamentally different from the conventional method of achieving single mode operation by modifying the mirror loss of different modes as in distributed Bragg reflector (DBR) lasers, or the group velocity as in distributed feedback (DFB) lasers. We showed that integration of gratings on microring laser cavities enables small footprint single mode lasers with lithographically defined emission wavelengths. We expect further reduction of the threshold current and increase of the output power by optimizing the device design and the fabrication process.

Appendix A: Analysis of radiation from a microring resonator with a permittivity perturbation using the multipole expansion method

Here we show that a permittivity perturbation to a microring resonator can be modeled as an equivalent volume current density, and that the radiated power is given by Eq. (2). We assume that the microring is pumped and the mode of interest at frequency ω has enough gain for lasing. At this resonant frequency, the electric and magnetic fields satisfy Maxwell's equations

$$\nabla \times \mathbf{E} = -j\omega\mu_0\mathbf{H}, \tag{3a}$$

$$\nabla \times \mathbf{H} = j\omega\varepsilon_0\varepsilon_r\mathbf{E} + \mathbf{J}, \tag{3b}$$

where ε_r is the spatially varying relative permittivity of the plain microring and $\mathbf{J}$ is the equivalent current density which is defined as

$$\mathbf{J} = j\omega\varepsilon_0(\varepsilon_{rp} - \varepsilon_r)\mathbf{E}, \tag{4}$$

and ε_{rp} represents the spatially varying permittivity of the perturbed microring (as shown in Fig. 1).

We assume that the microring radiates in free space and the smallest sphere that encloses the microring and the permittivity perturbation has a radius of R. We choose the coordinate system's origin at the center of the microring, and its z axis perpendicular to the plane of the microring. With these assumptions, the current is nonzero only over the region occupied by

#231409 - $15.00 USD Received 26 Dec 2014; revised 6 Feb 2015; accepted 6 Feb 2015; published 20 Feb 2015

the perturbation, which is enclosed by the virtual sphere. Outside of this sphere, the fields are a solution to the source free Maxwell's equations and can be expanded in terms of fields of multipoles as [28]

$$\mathbf{E} = \sum_{l=1}^{\infty} \sum_{m=-l}^{l} a_{lm} \mathbf{E}_{lm}^{\mathrm{TM}} + b_{lm} \mathbf{E}_{lm}^{\mathrm{TE}}, \tag{5a}$$

$$\mathbf{H} = \frac{1}{\eta_0} \sum_{l=1}^{\infty} \sum_{m=-l}^{l} a_{lm} \mathbf{E}_{lm}^{\mathrm{TE}} - b_{lm} \mathbf{E}_{lm}^{\mathrm{TM}}, \tag{5b}$$

where $\mathbf{E}_{lm}^{\mathrm{TM}}$ and $\mathbf{E}_{lm}^{\mathrm{TE}}$ respectively represent the electric fields of the TM and TE multipole of order (l,m) whose analytical expressions are presented in Appendix B. The coefficients a_{lm} and b_{lm} in Eqs. (5a) and (5b) are the coefficients of the transverse magnetic (TM) and transverse electric (TE) multipoles, respectively, and can be obtained by projecting the volume current density onto an orthogonal vectorial set [29]

$$a_{lm} = \int_{\mathscr{V}} \mathbf{J} \cdot \mathbf{U}_{lm}^{*} \mathrm{d}v, \tag{6a}$$

$$b_{lm} = \int_{\mathscr{V}} \mathbf{J} \cdot \mathbf{V}_{lm}^{*} \mathrm{d}v, \tag{6b}$$

where $\mathscr{V}$ represents the volume of the virtual sphere, and $\mathbf{U}_{lm}$ and $\mathbf{V}_{lm}$ are vector functions given analytically in Appendix B. It can be verified that $\mathbf{U}_{lm}$ and $\mathbf{V}_{l'm'}$ are mutually orthogonal, that is

$$\int_{\mathscr{V}} \mathbf{U}_{lm} \cdot \mathbf{V}_{l'm'}^{*} \mathrm{d}v = 0, \tag{7a}$$

$$\int_{\mathscr{V}} \mathbf{U}_{lm} \cdot \mathbf{U}_{l'm'}^{*} \mathrm{d}v = \delta_{ll'} \delta_{mm'} ||\mathbf{U}_{lm}||^2, \tag{7b}$$

$$\int_{\mathscr{V}} \mathbf{V}_{lm} \cdot \mathbf{V}_{l'm'}^{*} \mathrm{d}v = \delta_{ll'} \delta_{mm'} ||\mathbf{V}_{lm}||^2, \tag{7c}$$

where δ_{ij} is the Kronecker's delta function which is nonzero only when $i = j$ and in this case it is equal to 1. $||\mathbf{U}_{lm}||$ and $||\mathbf{V}_{lm}||$ are the L^2 norms of $\mathbf{U}_{lm}$ and $\mathbf{V}_{lm}$, respectively. These norms are independent of m and are given in Appendix B. It should be noted that although $\mathbf{U}_{lm}$ and $\mathbf{V}_{lm}$ constitute a set of mutually orthogonal vectorial functions, they do not form a complete set. Therefore, we can write the volume current density $\mathbf{J}$ as the summation of two parts: its projection on the space spanned by $\mathbf{U}_{lm}$ and $\mathbf{V}_{lm}$, and a part which is orthogonal to this space, that is

$$\begin{aligned} \mathbf{J} &= \sum_{l=1}^{\infty} \sum_{m=-l}^{l} \left(a_{lm} \frac{\mathbf{U}_{lm}}{||\mathbf{U}_{lm}||^2} + b_{lm} \frac{\mathbf{V}_{lm}}{||\mathbf{V}_{lm}||^2} \right) + \mathbf{J}' \\ &= \sum_{l=1}^{\infty} \sum_{m=-l}^{l} (\mathbf{J}_{lm}^{\mathrm{TM}} + \mathbf{J}_{lm}^{\mathrm{TE}}) + \mathbf{J}', \end{aligned} \tag{8}$$

where $\mathbf{J}'$ is orthogonal to $\mathbf{U}_{lm}$ and $\mathbf{V}_{lm}$

$$\int_{\mathscr{V}} \mathbf{J}' \cdot \left\{ \begin{array}{c} \mathbf{U}_{lm}^{*} \\ \mathbf{V}_{lm}^{*} \end{array} \right\} \mathrm{d}v = 0. \tag{9}$$

$\mathbf{J}'$ is the non-radiating part of the equivalent current density. The fields generated by $\mathbf{J}'$ vanish at any point outside the sphere volume $\mathscr{V}$, and $\mathbf{J}'$ excites neither TM nor TE waves outside of the sphere. More discussion on non-radiating current densities can be found in [30].

#231409 - $15.00 USD Received 26 Dec 2014; revised 6 Feb 2015; accepted 6 Feb 2015; published 20 Feb 2015

The total radiated power can be found using Eqs. (5a) and (5b) by integration of Poynting's vector [28]

$$P = \frac{Z_0}{2k^2}\sum_{l=1}^{\infty}\sum_{m=-l}^{l}|a_{lm}|^2+|b_{lm}|^2 = \sum_{l=1}^{\infty}\sum_{m=-l}^{l}P_{lm}^{\mathrm{TM}}+P_{lm}^{\mathrm{TE}}, \tag{10}$$

where Z_0 is the impedance of free space.

Using Eqs. (8)–(10), we can relate the radiated power of each mode to the norm of the component of the volume current density corresponding to that mode as

$$P_{lm}^{\mathrm{TM/TE}} = \frac{1}{2}R_l^{\mathrm{TM/TE}}I_{lm}^{\mathrm{TM/TE}^2}, \tag{11}$$

where we have defined

$$I_{lm}^{\mathrm{TM/TE}^2} \triangleq \lambda\int_{\mathscr{V}}|\mathbf{J}_{lm}^{\mathrm{TM/TE}}|^2\mathrm{d}v, \tag{12a}$$

$$R_l^{\mathrm{TM/TE}} \triangleq \frac{\eta_0}{2\pi k}\times\begin{cases}||\mathbf{U}_{lm}||^2 & \text{for TM}\\ ||\mathbf{V}_{lm}||^2 & \text{for TE}\end{cases}. \tag{12b}$$

Appendix B: Analytical expressions for multipole expansion

In this appendix, we present analytical expressions for the basis functions of the fields and for the volume current density for the multipole expansion. The basis functions for the TM and TE electric fields are given analytically as

$$\mathbf{E}_{lm}^{\mathrm{TM}} = \frac{-j\eta_0}{k\sqrt{l(l+1)}}\nabla\times\left(\mathrm{h}_l^{(2)}(kr)\mathbf{L}\mathrm{Y}_l^m\right), \tag{13a}$$

$$\mathbf{E}_{lm}^{\mathrm{TE}} = \frac{\eta_0}{\sqrt{l(l+1)}}\mathrm{h}_l^{(2)}(kr)\mathbf{L}\mathrm{Y}_l^m, \tag{13b}$$

where $\mathrm{h}_l^{(2)}(\cdot)$ is the spherical Hankel function of the second kind. $\mathrm{Y}_l^m(\theta,\phi)$ are the spherical harmonics

$$\mathrm{Y}_l^m(\theta,\phi) = \sqrt{\frac{2l+1}{4\pi}\frac{(l-m)!}{(l+m)!}}\,\mathrm{P}_l^m(\cos\theta)e^{-jm\phi}, \tag{14}$$

where $\mathrm{P}_l^m(\cdot)$ is the associated Legendre polynomial, and $\mathbf{L}$ is the orbital angular momentum operator which is defined as

$$\mathbf{L} = j\mathbf{r}\times\nabla = \frac{-j}{\sin\theta}\frac{\partial}{\partial\phi}\hat{\theta}+j\frac{\partial}{\partial\theta}\hat{\phi}. \tag{15}$$

The basis functions for the volume current expansion are given analytically as

$$\mathbf{U}_{lm} \triangleq \frac{k}{\sqrt{l(l+1)}}\frac{\partial}{\partial r}(r\mathrm{j}_l(kr))\nabla\mathrm{Y}_l^m+\frac{k\sqrt{l(l+1)}}{r}\mathrm{j}_l(kr)\mathrm{Y}_l^m\hat{r}, \tag{16a}$$

$$\mathbf{V}_{lm} \triangleq \frac{jk^2}{\sqrt{l(l+1)}}\mathrm{j}_l(kr)\nabla\mathrm{Y}_l^m\times\mathbf{r}. \tag{16b}$$

Their corresponding norms can be found via integration as

$$||\mathbf{U}_{lm}||^2 = \frac{k\pi}{2}\int_0^{kR}\frac{l(l+1)\mathrm{J}_{l+\frac{1}{2}}^2(u)+\left(u\mathrm{J}_{l-\frac{1}{2}}(u)-l\mathrm{J}_{l+\frac{1}{2}}(u)\right)^2}{u}\mathrm{d}u, \tag{17a}$$

$$||\mathbf{V}_{lm}||^2 = \frac{k\pi}{4}(kR)^2\left(\mathrm{J}_{l+\frac{1}{2}}^2(kR)-\mathrm{J}_{l+\frac{3}{2}}(kR)\mathrm{J}_{l-\frac{1}{2}}(kR)\right). \tag{17b}$$

#231409 - $15.00 USD Received 26 Dec 2014; revised 6 Feb 2015; accepted 6 Feb 2015; published 20 Feb 2015

Acknowledgments

This work was supported by the National Science Foundation (CAREER award ECCS-1055941).

#231409 - $15.00 USD Received 26 Dec 2014; revised 6 Feb 2015; accepted 6 Feb 2015; published 20 Feb 2015